Observational Signatures of Tearing Instability in the Current Sheet of a Solar Flare

Lei Lu [iD],[1,2] Li Feng,[3] Alexander Warmuth,[4] Astrid M. Veronig,[5] Jing Huang,[6] Siming Liu,[7] Weiqun Gan,[3] Zongjun Ning,[3] Beili Ying,[3] and Guannan Gao[8]

[1]*Key Laboratory of Dark Matter and Space Astronomy, Purple Mountain Observatory, CAS, Nanjing 210033, PR China*

[2]*CAS Key Laboratory of Solar Activity, National Astronomical Observatories, Beijing 100101, China*

[3]*Key Laboratory of Dark Matter and Space Astronomy, Purple Mountain Observatory, Chinese Academy of Sciences, 210033 Nanjing, China*

[4]*Leibniz-Institut für Astrophysik Potsdam (AIP), An der Sternwarte 16, 14482 Potsdam, Germany*

[5]*Institute of Physics & Kanzelhöhe Observatory for Solar and Environmental Research, University of Graz, 8010 Graz, Austria*

[6]*CAS Key Laboratory of Solar Activity, National Astronomical Observatories, 100012 Beijing, China*

[7]*School of Physical Science and Technology, Southwest Jiaotong University, Chengdu 610031, China*

[8]*Yunnan Observatories, Chinese Academy of Sciences, 650011 Kunming, China*

ABSTRACT

Magnetic reconnection is a fundamental physical process converting magnetic energy into not only plasma energy but also particle energy in various astrophysical phenomena. In this letter, we show a unique dataset of a solar flare where various plasmoids were formed by a continually stretched current sheet. EUV images captured reconnection inflows, outflows, and particularly the recurring plasma blobs (plasmoids). X-ray images reveal nonthermal emission sources at the lower end of the current sheet, presumably as large plasmoids with a sufficiently amount of energetic electrons trapped in. In

Corresponding author: Li Feng
lfeng@pmo.ac.cn

the radio domain, an upward slowly drifting pulsation structure, followed by a rare pair of oppositely drifting structures, was observed. These structures are supposed to map the evolution of the primary and the secondary plasmoids formed in the current sheet. Our results on plasmoids at different locations and scales shed important light on the dynamics, plasma heating, particle acceleration, and transport processes in the turbulent current sheet and provide observational evidence for the cascading magnetic reconnection process.

Keywords: magnetic reconnection — methods: data analysis — Sun: flares — Sun: radio radiation

1. INTRODUCTION

Magnetic reconnection is a fundamental process in plasma physics that is relevant not only in the context of solar and stellar flares, but also in planetary magnetospheres, magnetars, accretion disks, and in laboratory plasmas (Priest & Forbes 2000; Lin et al. 2008; Zweibel & Yamada 2009). It was first proposed and has been widely used to explain the energy release in solar eruptions (Su et al. 2013; Li et al. 2016; Cairns et al. 2018; Gou et al. 2019). In the classical CSHKP model (Carmichael 1964; Sturrock 1966; Hirayama 1974; Kopp & Pneuman 1976), a closed magnetic structure is stretched by a rising flux rope (usually observed as a filament), forming a current sheet (CS) where oppositely directed magnetic field lines flow in and reconnect. The energy pre-stored in the magnetic field is then converted into various energy forms such as heating of plasma, acceleration of particles, bulk mass motions, and emissions in almost all wavelengths. The newly formed field lines retract both downward and upward from the reconnection site, forming post-flare loops and coronal mass ejections (CMEs). The CSHKP model agrees well with the large-scale dynamics of the observed eruptive events. However, the reconnection rate estimated from the model is often found to be too low to explain the rapid energy release in solar flares (Shibata & Magara 2011). Moreover, with a single diffusion (reconnection) region, the CSHKP model also shows an apparent inability to account

for the acceleration of the observed large number of energetic particles (Fletcher 2005; Krucker et al. 2008).

Because of these difficulties, a scenario of cascading reconnection was suggested by Shibata & Tanuma (2001). In this scenario, the initial CS is continually stretched by the rising flux rope (CME), at some point the tearing-mode instability sets in and multiple magnetic islands (also called plasmoids) are formed, interleaved with thin CSs. The newly formed plasmoids are subjected to increasing separation, leading to the secondary tearing instability that causes the CSs to be further filamented. As the process continues, third and higher orders of tearing instabilities take place and plasmoids with smaller and smaller size are formed until the widths of the CSs reach the plasma-kinetic scales at which the magnetic energy is dissipated. This scenario was later supported by the analytical theory of chain plasmoid instability (Loureiro et al. 2007; Uzdensky et al. 2010) and confirmed by various numerical simulations (Samtaney et al. 2009; Bhattacharjee et al. 2009; Huang & Bhattacharjee 2010; Shen et al. 2011; Bárta et al. 2011; Mei et al. 2012; Ni et al. 2015; Mei et al. 2017; Li 2019; Zhao et al. 2021). It has been shown that the reconnection rate as well as the acceleration of solar particles can be significantly enhanced by the formation and ejection of the secondary and higher orders of plasmoids.

These theoretical predictions are consistent with laboratory modelling of secondary CSs in laser-plasma interaction (Dong et al. 2012) and in situ observations of a secondary magnetic island in the Earth's magnetotail (Wang et al. 2010). In solar eruptive events, the plasmoids were first recognized from soft X-ray images during the impulsive phase of a solar flare (Shibata et al. 1995). Later, they were also identified in hard X-ray, extreme ultraviolet (EUV), white light, and radio images (Hudson et al. 2001; Ko et al. 2003; Shimojo et al. 2017). Additionally, drifting pulsation structures (DPSs) which are sometimes observed in the solar radio dynamic spectra are also interpreted as signatures of plasmoids (Kliem et al. 2000; Karlický 2004; Liu et al. 2010). However, the formation of DPSs is a very complex process that requires many specific conditions. They can only be observed in some special cases. In this Letter, we present a unique dataset where the plasmoid formation

and evolution in a turbulent current sheet during magnetic reconnection are directly observed in unprecedented detail.

2. OBSERVATIONS AND ANALYSIS

The event of interest with clear observations of a current sheet occurred on July 19, 2012. Observations (the 131 Å passband) from the Atmospheric Imaging Assembly (AIA) (Lemen et al. 2012) on board Solar Dynamic Observatory (SDO) show that on July 18 a pre-existing flux rope (Fig. 1 a) became destabilized, impulsively accelerated (Fig. 1 b−c) and eventually evolved into a white-light CME. Behind the CME, a long vertical current sheet is formed, with its lower end connecting to the cusp-shaped flare loops. According to the peak soft X-ray (1−8 Å) flux (Fig. 4 a) recorded by the Geostationary Operational Environmental Satellites (GOES), the flare can be classified as an M7.7 flare. Previous studies have investigated different aspects of the event, for instance, the microwave imaging of the hot flux rope (Wu et al. 2016), a general timeline of the particle acceleration, plasma heating, dynamic processes in the current sheet (Liu et al. 2013; Sun et al. 2014; Liu 2013; Huang et al. 2016), properties of the above-the-loop-top hard X-ray sources (Krucker & Battaglia 2014; Oka et al. 2015), as well as formation of the related CME (Patsourakos et al. 2013). Taking advantage of the EUV, X-ray, and radio observations in synergy, here we are moving forward to the most comprehensive and direct observations of plasmoids formed in the current sheet.

The current sheet is found to be highly dynamic. Starting from about 05:13 UT, a blob-like structure (blob1) was observed to move upward with almost a constant speed of ~ 640 km s^{-1} (Fig. 1 d−i). Then at about 05:14:57 UT, another blob (blob2) appeared with an average speed of ~ 1180 km s^{-1} (Fig. 1 h−l). Different from blob1, blob2 moves fast at the beginning, and then slows down. Such blobs are interpreted as plasmoids, which are supposed to be generated due to the tearing instabilities of the continually stretched CS. After about 05:16 UT, the impulsive phase of the flare starts, showing a sudden increase of hard X-ray (25-50 keV) flux as measured by the Reuven Ramaty High Energy Solar Spectroscopic Imager (RHESSI) (Lin et al. 2002). Here the RHESSI thermal (6-12 keV) and nonthermal (25-50 keV) sources (Fig. 1 m-r) were reconstructed using the "clean" algorithm and detectors 3, 5, 6, 7, 8, 9. Depending on the count rate, the integration time for the reconstruction

ranges from 32 seconds during the flare impulsive phase to 2 minutes during the flare early and decay phases. Since the production of X-ray bremsstrahlung requires a certain level of target density, hard X-ray sources are commonly observed at low altitudes at the flare footpoints or above the loop top (cyan contours). The footpoint sources are generally thought to be produced by thick-target bremsstrahlung (or braking radiation) of energetic electrons stopped in the cold and dense solar atmosphere (Brown 1971; Hudson 1972). The above-the-loop-top sources from the corona, however, is still under much debate, and several ideas regarding their origin have been proposed (Masuda et al. 1994; Fletcher 1995; Karlický & Bárta 2011; Kong et al. 2019). One of them suggests that they can be interpreted as a result of successive merging of plasmoids above the flare loop top, during which a large plasmiod trapping a sufficient amount of energetic particles is formed (Karlický & Bárta 2011). As revealed in the magnetohydrodynammic and particle kinetic simulations (Kong et al. 2020), the other possibility of the above-the-loop-top sources is the non-thermal electrons accelerated around the up-moving termination shock due to the plasmoid-shock interactions.

To quantitatively investigate the dynamic process, we select two oblique slices in AIA images (S1 and S2 in Fig. 1 c), with S1 along the CS and S2 in its perpendicular direction. The time-distance plots clearly show that after the eruption of the flux rope, various plasmoids were formed and ejected along the trailing CS (Fig. 2 a), the ambient coronal plasma that is frozen in the magnetic field was first pushed aside (blue lines in Fig. 2 b), then possibly under the restoring force of the magnetic field, the cool plasma (visible in 171 Å, ~ 1 MK) on both sides keeps converging into the CS with an average velocity of about $16-50$ km s^{-1} (cyan lines in Fig. 2 b), and once they come into contact, the magnetic energy pre-stored in the plasma is impulsively released, observed as a sudden flux increase in hard X-ray (≥ 25 keV) and the time derivative of GOES 1-8 Å flux, according to which the flare impulsive phase is defined (Fig. 2 c). Note that, the start time of the flare impulsive phase is defined as a sudden rise of the RHESSI 25-50 keV flux while due to the RHESSI night, the end time is defined by the time derivative of GOES 1-8 Å flux according to the Neupert effect (Neupert 1968; Veronig et al. 2005). Meanwhile, the plasma is strikingly heated and outflow tracers such as
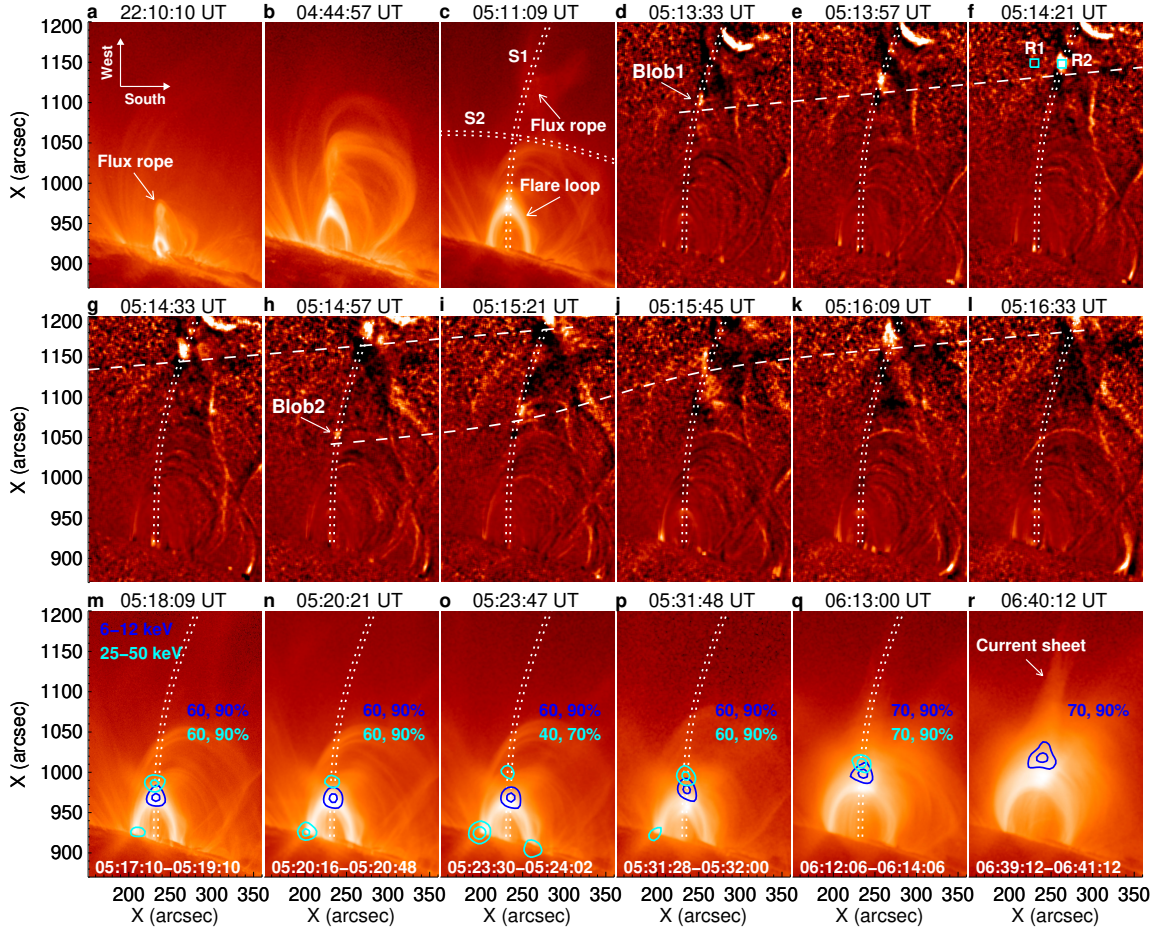
Figure 1. Snapshots of the eruption recorded by the 131 Å filter of SDO/AIA. West is rotated to the top and south to the right. Panel(a) shows the flux rope formed in an earlier confined C4.5 flare. Panels (b-r) show the eruption and evolution of the flux rope and the associated M7.7 flare. "S1" and "S2" in panel (c) indicate two slits placed along and perpendicular to the current sheet. Panels (d-l) are running ratio images, showing motions of two blob-like plasmoids. "R1"and "R2" in panel (f) indicate two subregions used for the DEM analysis. The arrow in panel (r) refers to the long current sheet. The contours overplotted in panels (m)-(r) show the RHESSI X-ray sources at 6-12 keV (blue) and 25-50 keV (cyan) reconstructed with the "clean" algorithm. The percentages define the contour levels.

fast upward-moving blobs and downward-shrinking loops become visible in AIA high temperature passband such as 131 Å (cyan lines in Fig. 2 a).

Fig. 3 (a) shows the intensity profile of AIA 131 Å along S1 at different times, with h1 and h2 indicating the upper and lower boundaries of blob1. The height (h=(h1+h2)/2) and size (s=h2-h1,
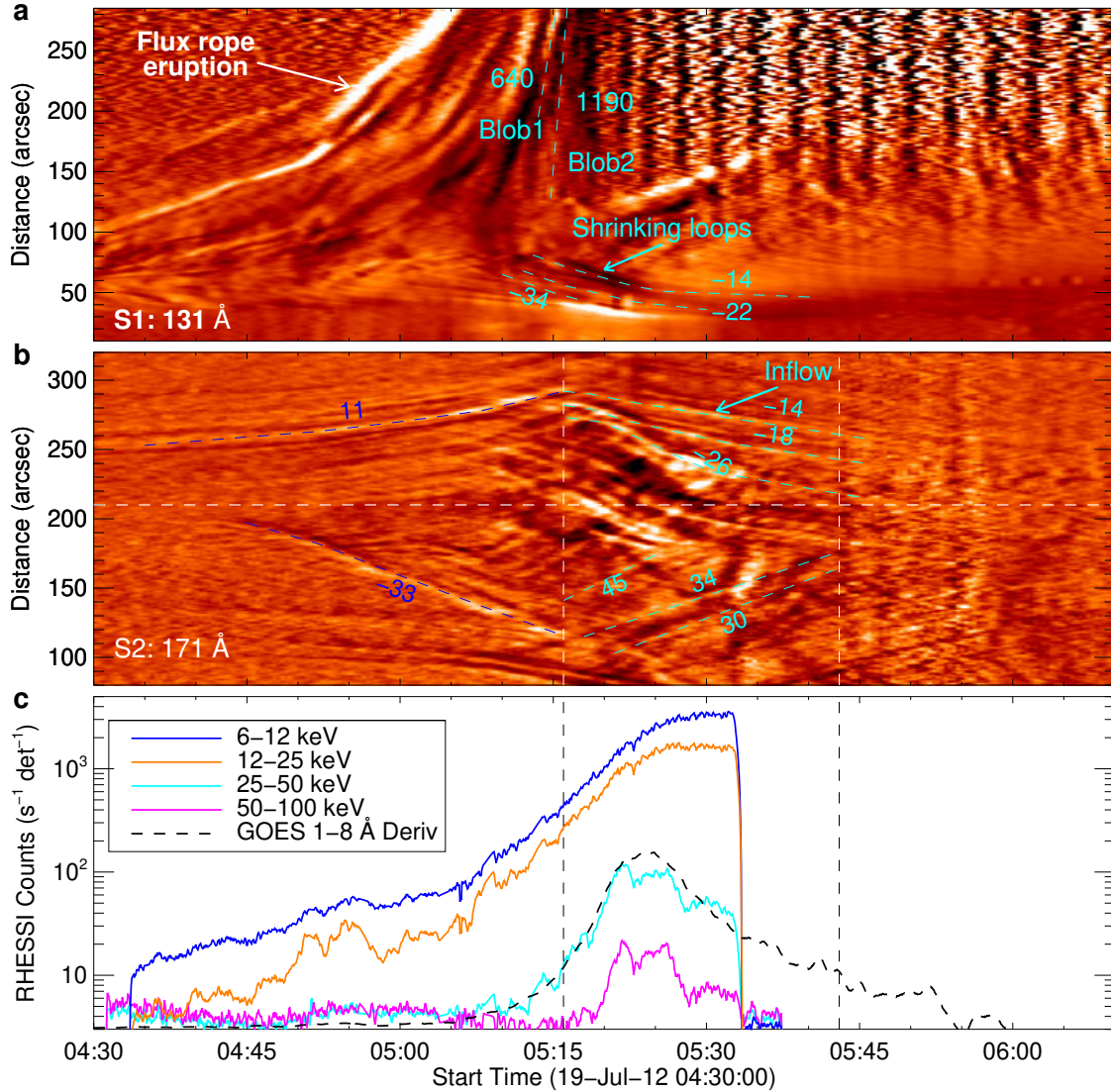
Figure 2. Temporal evolution of plasma inflows and outflows during the magnetic reconnection as observed in EUV by SDO/AIA. (a) Time-distance plot in AIA 131 Å along the current sheet (S1), showing the eruption of the flux rope and the bi-directional reconnection outflows. (b) Time-distance plot in AIA 171 Å along S2 (perpendicular to the current sheet), showing the separation (blue lines) and approach (cyan lines) of oppositely directed magnetic structures (the numbers denote the average speeds in units of km s^{-1}). The horizontal white dashed line denotes the position of the current sheet. (c) Time profiles of the RHESSI X-ray emission in different energy bands and time derivative of GOES flux in 1-8 Å . The two vertical dashed lines indicate the flare impulsive phase.

error bars) of the blob are shown in Fig. 3 (b). The average electron density (Fig 3 c) as well as

the average temperature (Fig 3 d) of the blob was estimated from the analysis of its differential emission measure (DEM) (see Appendix A for details). As the blob propagated radially outward, it expanded in size. This expansion is probably due to the ambient magnetic field decreasing with height. Meanwhile, the plasma electron density inside the blob correspondingly decreased. The temperature of the blob did not change significantly at the beginning (T $\sim$ 6.4 MK), but quickly rose to 7.7 MK after about 05:15 UT, implying that a number of suprathermal and/or nonthermal electrons may have been injected into the plasmoid and/or the plasmoid is locally energized and heated.

The plasmoid (blob1) left the field of view (FOV) of AIA at about 05:15:21 UT, and in about two minutes, a clear DPS event (hereafter, the initial DPS), was observed by Yunnan Astronomical Observatories Radio Spectrometers (Gao et al. 2014). The DPS consists of many narrow-band pulsation structures with a characteristic repetition time of about 200 seconds (Huang et al. 2016), and as a whole it drifts from high to low frequencies at a rate of about -0.68 $\pm$ 0.13 MHz s^{-1}, obtained from a linear fit to its upper and lower boundaries (Fig. 4 b). The magenta and white lines in Fig. 4 (b) represent the RHESSI hard X-ray (25-50 keV) time profile and the time derivative of the GOES 1-8 Å light curves, which show a rapid energy release during the DPS. Shortly after the initial DPS (from about 05:33:13 UT), a pair of oppositely drifting structures (hereafter, O-DSs) appeared (Fig. 4 c). The drift rates of the upper and lower branches of the O-DSs were estimated to be -1.96 $\pm$ 0.58 MHz s^{-1} and 1.22 $\pm$ 0.32 MHz s^{-1}, respectively. Similar oppositely drifting features were also reported by Karlický & Rybák (2020). According to previous studies (Kliem et al. 2000; Shibata & Tanuma 2001; Karlický et al. 2002; Karlický 2004), the initial DPS together with the subsequent O-DSs are supposed to map the evolution of the primary and secondary plasmoids that were formed due to the cascading tearing instabilities in the CS as it was continually stretched. These plasmoids were then exited by energetic electron beams accelerated during the magnetic reconnection process and producing radio emissions via plasma emission mechanism. Moreover, some narrow-band spike-like structures can be distinguished in between the oppositely drifting structures, which is suggestive
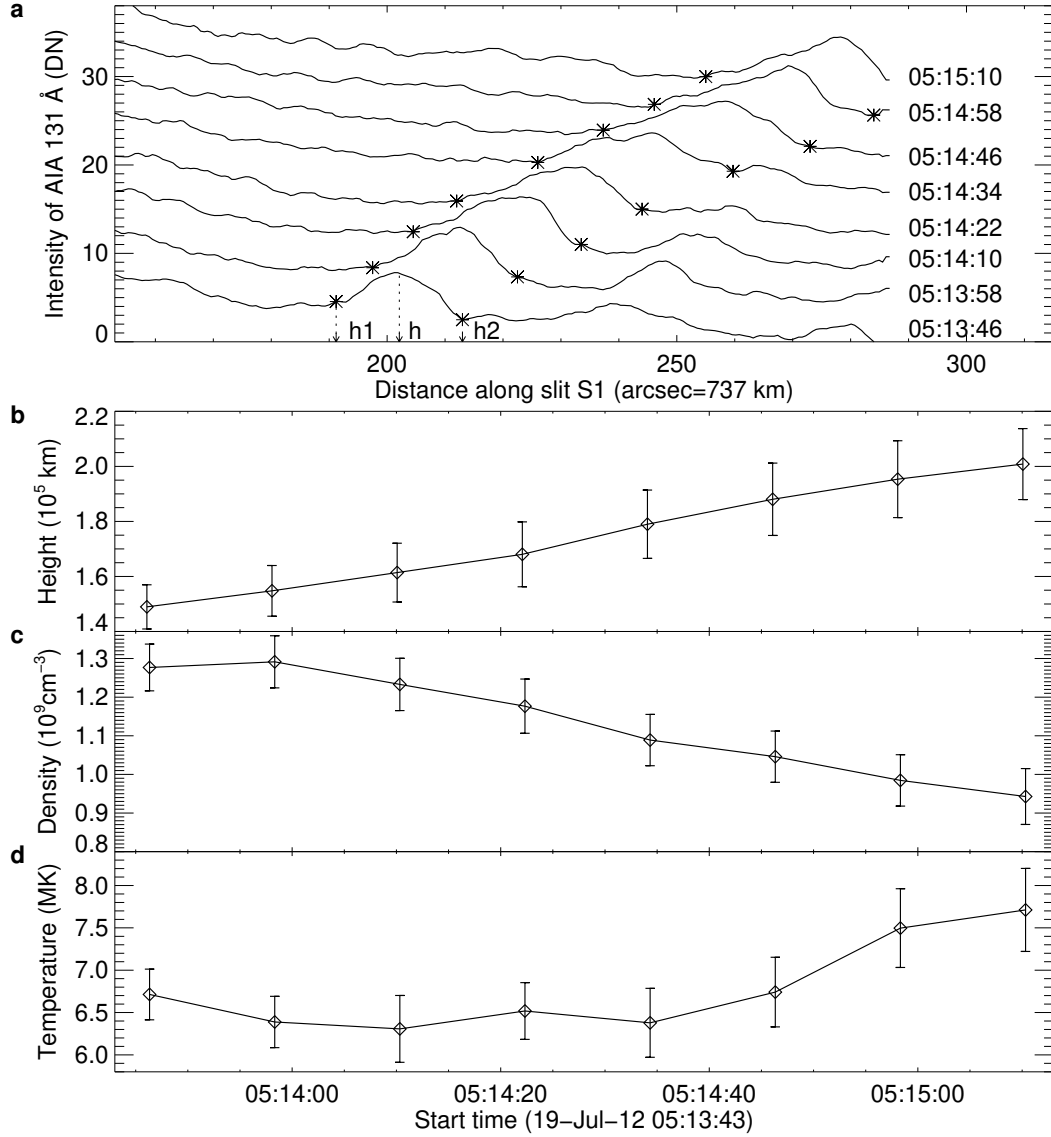
Figure 3. Temporal evolution of the physical parameters of Blob1. (a) Intensity distributions along S1 at eight selected times. The curves are shifted vertically to avoid overlap. "h1" and "h2" indicate the lower and upper boundaries of the blob. (b) Evolution of the blob height (h=(h1+h2)/2). The size (h2-h1) of the blob is regarded as the uncertainties (error bars). (c) The electron density inside the blob. (d) The DEM-weighted temperature of the blob. The error bars in (c) and (d) are obtained from 100 Monte Carlo simulations.

of the reconnection outflows being in a turbulent state (Bárta & Karlický 2001; Karlický & Bárta 2011; Zhao et al. 2018; Ye et al. 2019).

3. DISCUSSION
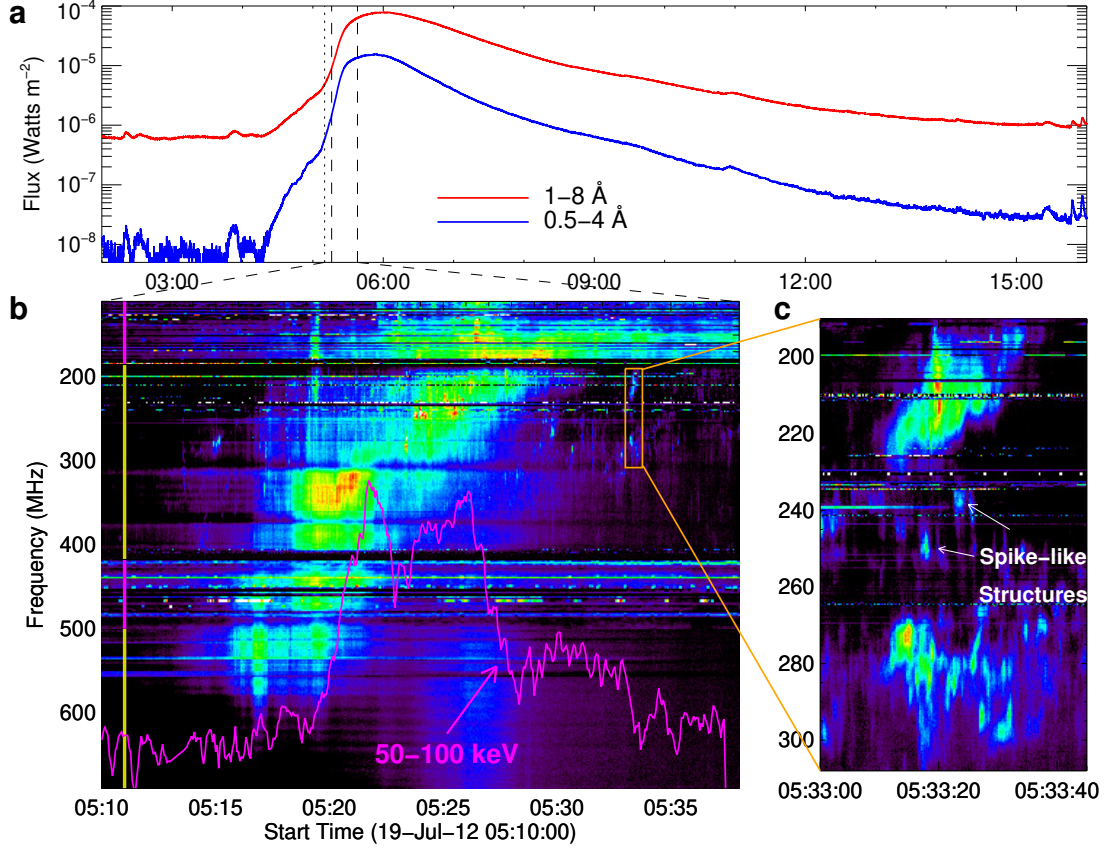
Figure 4. The X-ray and radio observations of the flare impulsive phase. (a) GOES soft X-ray fluxes in 1-8 Å (red line) and 0.5-4 Å (blue line), the two vertical dashed lines indicate the flare impulsive phase from 05:16 to 05:43 UT. (b) Combined radio dynamic spectra obtained by the Yunnan (yellow vertical bar) and Culgoora (magenta vertical bar) spectrographs, showing drifting pulsation structures (DPSs). The overplotted magenta and white light curves show the hard X-ray (50-100 keV) and time derivative of GOES 1-8 Å fluxes, respectively. (c) Zoomed-in view of a pair of oppositely drifting structures. The arrows points to some spike-like structures.

Generally it is assumed that these observed radio frequency f_{obs} is equal to the fundamental or second harmonic of the electron plasma frequency f_p inside a plasmoid, with f_p can be converted into the electron plasma density n_e via $f_p = 8980\sqrt{n_e}$. The electron density n_e, on the other hand, is usually related with the height of the plasmoid in the solar corona. Thus if we know how the density of the plasmoid varies with its height, we can estimate the kinetics of the radio-related plasmoids. Here we use a plasmoid density model derived by considering the balance of pressure inside and outside the plasmoid by Nishizuka et al. (2015) (see Appendix B for details). It is found that under

the assumption of the second harmonic plasma emission, the physical parameters (height and density) of the plasmoid inferred from the initial DPS are consistent with parameters of the blob1 observed in EUV images considering the two-minute measurement gap. Therefore, we suppose that the initial DPS is likely to be generated inside blob1 or the blob1-liked plasmoid. This could also be supported by the sudden temperature increase of blob1 (implying energetic electron injection) near the early phase of the radio emission. Based on the drift rate of the DPS, the velocity of the related plasmoid is estimated to be about 486 km s^{-1}, which is smaller than that observed in EUV images, implying deceleration of blob1 after it left the FOV of AIA. Again under the assumption of second harmonic plasma emission, the starting heights of the oppositely drifting plasmoids (the O-DSs) were estimated to be about 3.4×10^5 km and 3.1×10^5 km, respectively. At these large heights we are not able to identify the EUV counterparts in AIA images, since the AIA field-of-view is too small. The velocity of the downward plasmoid (~ 508 km s^{-1}) is much smaller than that of the upward plasmoid (~ 1035 km s^{-1}), implying that the downward plasmoids are subject to more resistance than the upward ones.

4. SUMMARY

In summary, the multi-waveband and high-resolution observations in EUV, X-ray, and radio of the flare allow us to investigate the plasmoids at the vertical current sheet behind an erupting flux rope in great detail. The plasmoids were first observed as upward-moving blob-like structures in EUV images during the early phase of the flare. Then with the onset of the flare impulsive phase, a large number of electron beams were accelerated, which can excite the plasmoids to oscillate and produce radio emission through plasma emission mechanism or hard X-ray emission via the bremsstrahlung mechanism. Since energetic electrons require a certain level of target density for the production of nonthermal hard X-ray, hard X-ray sources were only observed near the lower end of the CS (i.e., the above-the-loop-top hard X-ray sources). Meanwhile a strong DPS, followed by a rare pair of oppositely drifting structures, were clearly observed from radio dynamic spectra. According to previous studies (Ohyama & Shibata 1998; Kliem et al. 2000; Karlický 2004), these structures were supposed to map the evolution of the primary and secondary plasmoids generated

due to the tearing instabilities in the current sheet. Based on the observations, we have compared the physical properties of the plasmoids at different stages and found that the initial DPS might evolve from the blob1 seen in AIA images. The aforementioned analyses show that there are multiple small-scale short-lived dissipative regions at multiple X lines. Therefore the energy release during the magnetic reconnection occurs probably in a fragmented manner. These results are consistent with theoretical prediction of the plasmoid generation by an unstable CS, and support the concept of cascading reconnection. All these findings help us to obtain a deeper understanding of the magnetic reconnection processes which are the engine of solar eruptions, and shed lights on the energy release in other astrophysics processes.

APPENDIX

In this supplemental material, we provide technical details of main results in the main text.

A. DIFFERENTIAL EMISSION MEASURE RECONSTRUCTION

The differential emission measure (DEM) is a physical quantity that measures the amount of materials emitting at a certain temperature T. Assuming an optically-thin coronal plasma, the DEM can be related to the narrow-band EUV (or broadband X-ray) observations y_i as

$$y_i = \int K_i(T) \, \text{DEM}(T) dT + \delta y_i, \tag{A1}$$

where $K_i(T)$ is the temperature response function which can be computed using the CHIANTI package(Landi et al. 2013), δy_i represents a random error that involved in a measurement. Using the observations in AIA's six EUV passbands that are centred on iron emission lines (94 Å, 131 Å, 171 Å, 193 Å, 211 Å, and 335 Å), the DEM(T) can be inverted. The procedure we use is *xrt_dem_iterative2.pro*, which is available in the Solar Software (SSW) package. In the supplementary Fig. S1, we show 100 Monte Carlo (MC) simulations of the DEM distributions (for each MC, a small random error is added to the observations). The black line represents the best-fit DEM distribution.

The total emission measure EM and the DEM-weighted temperature T_{mean} are calculated via the following equations:

$$\text{EM} = \int_{T_{min}}^{T_{max}} \text{DEM}(T) dT, \tag{A2}$$

$$T_{mean} = \frac{\int_{T_{min}}^{T_{max}} \text{DEM}(T) T dT}{\int_{T_{min}}^{T_{max}} \text{DEM}(T) dT}, \tag{A3}$$

The temperature range is set to be $6.0 \leq \log T \leq 6.5$ for the quiet corona and $6.0 \leq logT \leq 7.3$ for the plasmoid, within which the DEM is well constrained (see Fig. S1). The average electron plasma density inside the plasmoid is deduced via,

$$n_e = \sqrt{\frac{\text{EM}}{l}} \quad [\text{cm}^{-3}] \tag{A4}$$

where l represents the effective depth along the line of sight. We assumed that the plasmoid has a similar extent in depth and in length. The length of the plasmoid is shown by the error bars in Fig. 3(b), from which we estimate its average value of $\sim 2.4 \times 10^9$ cm. Three standard deviations
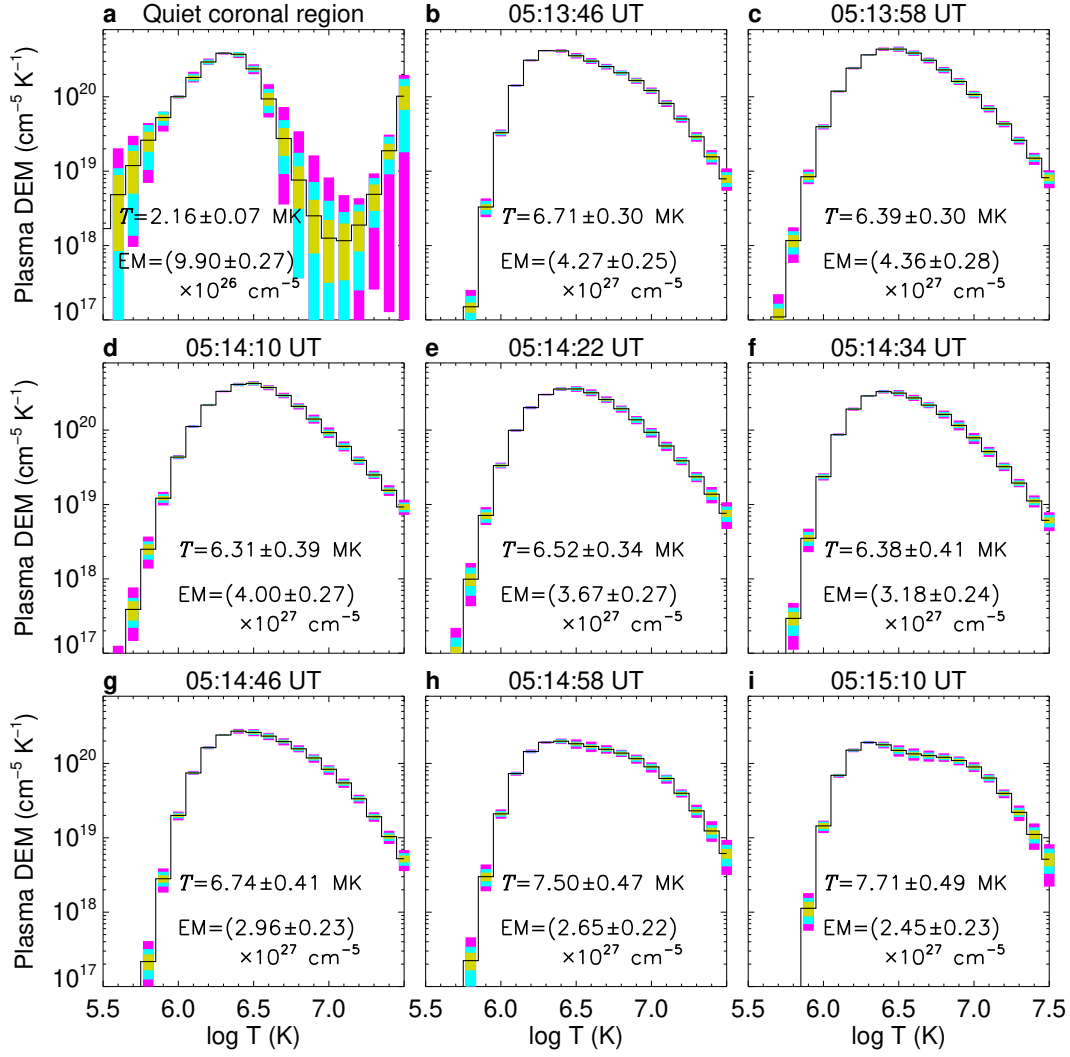
Figure S1. Panel (a): DEM of the quiet coronal region (R1 in Fig. 1g), Panels (b-i): DEM of the blob region (R2 in Fig. 1g) at eight selected times. The yellow, cyan and purple colors represent regions in which 50%, 80% and 95% of 100 Monte Carlo (MC) solutions are contained, respectively. The black line represents the best-fit DEM distribution. The total emission measure and the DEM-weighted temperatures are given in each panel. Three standard deviations (3σ) of the 100 Monte Carlo simulations are regarded as the uncertainties.

(3σ) of 100 Monte Carlo simulations away from the best fit are considered as the uncertainties of the temperature, EM and electron density for the plasmoid (see error bars in Fig. 3c-d).

B. PLASMOID DENSITY MODEL

The plasmoid density model, i.e., the variance of the electron density inside the plasmoid n_{in} with its height h in the solar corona, is derived by considering the balance of pressure inside and outside the plasmoid by Nishizuka et al. (2015). The gas and magnetic pressure outside the plasmoid are estimated by assuming a plasma density model and a dipolar global magnetic field, respectively. Here we only give the derived expression(see Nishizuka et al. (2015) for details):

$$
n_{in}(h) = \begin{cases} n_1(\dfrac{h_1}{h})^p \dfrac{T_{out}}{T_{in}} + \dfrac{B_0^2}{8\pi 2k_B T_{in}}(1+\dfrac{h}{h_D})^{-6}, & (h \le h_1) \\ n_Q exp(-\dfrac{h}{\lambda_T})\dfrac{T_{out}}{T_{in}} + \dfrac{B_0^2}{8\pi 2k_B T_{in}}(1+\dfrac{h}{h_D})^{-6}, & (h \ge h_1) \end{cases}
$$

where $h_1 = 1.6 \times 10^{10}$ cm is the transition height between the lower and the higher corona, $p = 2.38$ is the power-law index, $n_1 = 4.6 \times 10^7 \, cm^{-3}$, $n_Q = 4.6 \times 10^8 \, cm^{-3}$ are the base densities, $k_B = 1.38 \times 10^{-23} \, J/K$ is the Boltzmann constant, and $\lambda_T = RT/g = 6.9 \times 10^9$ cm is the density scale. $B_0 = 100$ G and $h_D = 7.5 \times 10^8$ cm are two parameters used to estimate the coronal magnetic field. T_{in} and T_{out} represent temperatures inside and outside the plasmoid, which are obtained from our DEM results.

The maximal and minimal electron density n_{max} and n_{min} derived from the frequency range of the DPS are then converted into the minimal and maximal heights h_{min} and h_{max} of the plasmoid. Subsequently, the height and size of the plasmoid are obtained from $h = (h_{max} + h_{min})/2$, and $W_{pla} = h_{max} - h_{min}$.

For each DPS in Fig. 4, two time instances are selected for calculation. The supplementary Table S1 shows the physical parameters of the related plasmoids inferred by assuming both fundamental (the bracketed values) and second harmonic plasma emission. As can be seen, comparing to the results with the fundamental plasma emission assumption, the results calculated by assuming the second harmonic plasma emission reveal a higher plasma density and smaller coronal height of the related plasmoid.

REFERENCES

Bárta, M., Büchner, J., Karlický, M., & Skála, J. 2011, ApJ, 737, 24, doi: 10.1088/0004-637X/737/1/24

Bárta, M., & Karlický, M. 2001, A&A, 379, 1045, doi: 10.1051/0004-6361:20011375

LU ET AL.

Table S1. Radio-inferred parameters of the plasmoid.

Radio Features	the Initial DPS		DS-upper		DS-lower	
Time (UT)	05:17:00	05:24:00	05:33:14	05:33:20	05:33:14	05:33:20
f_{max} (MHz)	610	360	230	225	285	293
f_{min} (MHz)	420	110	212	195	267	275
n_{max} (10^8 cm^{-3})	11.5(46.1)	4.02(16.1)	1.64(6.56)	1.57(6.28)	2.52(10.1)	2.66(10.6)
n_{min} (10^8 cm^{-3})	5.47(21.9)	0.38(1.50)	1.39(5.57)	1.18(4.72)	2.21(8.84)	2.34(9.38)
h_{min} (10^5 km)	2.41(1.88)	2.95(2.27)	3.34(2.63)	3.36(2.65)	3.10(2.44)	3.07(2.42)
h_{max} (10^5 km)	2.78(2.15)	6.32(3.67)	3.43(2.71)	3.53(2.78)	3.17(2.50)	3.14(2.47)
h_{pla} (10^5 km)	2.59(2.02)	4.64(2.97)	3.38(2.67)	3.44(2.72)	3.13(2.47)	3.10(2.45)
W_{pla} (10^4 km)	3.62(2.66)	33.7(14.0)	0.94(0.75)	1.68(1.33)	0.70(0.55)	0.67(0.53)
v_{pla} (kms^{-1})	486(227)		1035(822)		−508(−403)	

Notes. "DS-upper" means the upper branch (drifting towards lower frequencies) and "DS-lower" means the lower branch (drifting towards higher frequencies) of the oppositely drifting structures. f_{max} and f_{min} are the high and low frequency cutoffs. By default, the values are computed by assuming the second harmonic plasma emission. The bracketed values indicate the results calculated with the fundamental plasma emission assumption.

Bhattacharjee, A., Huang, Y.-M., Yang, H., & Rogers, B. 2009, Physics of Plasmas, 16, 112102, doi: 10.1063/1.3264103

Brown, J. C. 1971, SoPh, 18, 489, doi: 10.1007/BF00149070

Cairns, I. H., Lobzin, V. V., Donea, A., et al. 2018, Scientific Reports, 8, 1676, doi: 10.1038/s41598-018-19195-3

Carmichael, H. 1964, NASA Special Publication, 50, 451

Dong, Q.-L., Wang, S.-J., Lu, Q.-M., et al. 2012, PhRvL, 108, 215001, doi: 10.1103/PhysRevLett.108.215001

Fletcher, L. 1995, A&A, 303, L9

—. 2005, SSRv, 121, 141, doi: 10.1007/s11214-006-7181-7

Gao, G., Wang, M., Dong, L., Wu, N., & Lin, J. 2014, NewA, 30, 68, doi: 10.1016/j.newast.2014.01.008

Gou, T., Liu, R., Kliem, B., Wang, Y., & Veronig, A. M. 2019, Science Advances, 5, 7004, doi: 10.1126/sciadv.aau7004

Hirayama, T. 1974, SoPh, 34, 323, doi: 10.1007/BF00153671

Huang, J., Kontar, E. P., Nakariakov, V. M., & Gao, G. 2016, ApJ, 831, 119, doi: 10.3847/0004-637X/831/2/119

Huang, Y.-M., & Bhattacharjee, A. 2010, Physics of Plasmas, 17, 062104, doi: 10.1063/1.3420208

Hudson, H. S. 1972, SoPh, 24, 414, doi: 10.1007/BF00153384

Hudson, H. S., Kosugi, T., Nitta, N. V., & Shimojo, M. 2001, ApJL, 561, L211, doi: 10.1086/324760

Karlický, M. 2004, A&A, 417, 325, doi: 10.1051/0004-6361:20034249

Karlický, M., & Bárta, M. 2011, ApJ, 733, 107, doi: 10.1088/0004-637X/733/2/107

Karlický, M., Fárník, F., & Mészárosová, H. 2002, A&A, 395, 677, doi: 10.1051/0004-6361:20021310

Karlický, M., & Rybák, J. 2020, ApJS, 250, 31, doi: 10.3847/1538-4365/abb19f

Kliem, B., Karlický, M., & Benz, A. O. 2000, A&A, 360, 715

Ko, Y.-K., Raymond, J. C., Lin, J., et al. 2003, ApJ, 594, 1068, doi: 10.1086/376982

Kong, X., Guo, F., Shen, C., et al. 2020, ApJL, 905, L16, doi: 10.3847/2041-8213/abcbf5

—. 2019, ApJL, 887, L37, doi: 10.3847/2041-8213/ab5f67

Kopp, R. A., & Pneuman, G. W. 1976, SoPh, 50, 85, doi: 10.1007/BF00206193

Krucker, S., & Battaglia, M. 2014, ApJ, 780, 107, doi: 10.1088/0004-637X/780/1/107

Krucker, S., Battaglia, M., Cargill, P. J., et al. 2008, A&A Rv, 16, 155, doi: 10.1007/s00159-008-0014-9

Landi, E., Young, P. R., Dere, K. P., Del Zanna, G., & Mason, H. E. 2013, ApJ, 763, 86, doi: 10.1088/0004-637X/763/2/86

Lemen, J. R., Title, A. M., Akin, D. J., et al. 2012, SoPh, 275, 17, doi: 10.1007/s11207-011-9776-8

Li, D. 2019, Research in Astronomy and Astrophysics, 19, 067, doi: 10.1088/1674-4527/19/5/67

Li, L., Zhang, J., Peter, H., et al. 2016, Nature Physics, 12, 847, doi: 10.1038/nphys3768

Lin, J., Cranmer, S. R., & Farrugia, C. J. 2008, Journal of Geophysical Research (Space Physics), 113, A11107, doi: 10.1029/2008JA013409

Lin, R. P., Dennis, B. R., Hurford, G. J., et al. 2002, SoPh, 210, 3, doi: 10.1023/A:1022428818870

Liu, R. 2013, MNRAS, 434, 1309, doi: 10.1093/mnras/stt1090

Liu, R., Lee, J., Wang, T., et al. 2010, ApJL, 723, L28, doi: 10.1088/2041-8205/723/1/L28

Liu, W., Chen, Q., & Petrosian, V. 2013, ApJ, 767, 168, doi: 10.1088/0004-637X/767/2/168

Loureiro, N. F., Schekochihin, A. A., & Cowley, S. C. 2007, Physics of Plasmas, 14, 100703, doi: 10.1063/1.2783986

Masuda, S., Kosugi, T., Hara, H., Tsuneta, S., & Ogawara, Y. 1994, Nature, 371, 495, doi: 10.1038/371495a0

Mei, Z., Shen, C., Wu, N., et al. 2012, MNRAS, 425, 2824, doi: 10.1111/j.1365-2966.2012.21625.x

Mei, Z. X., Keppens, R., Roussev, I. I., & Lin, J. 2017, A&A, 604, L7, doi: 10.1051/0004-6361/201731146

Neupert, W. M. 1968, ApJL, 153, L59, doi: 10.1086/180220

Ni, L., Kliem, B., Lin, J., & Wu, N. 2015, ApJ, 799, 79, doi: 10.1088/0004-637X/799/1/79

Nishizuka, N., Karlický, M., Janvier, M., & Bárta, M. 2015, ApJ, 799, 126, doi: 10.1088/0004-637X/799/2/126

Ohyama, M., & Shibata, K. 1998, ApJ, 499, 934, doi: 10.1086/305652

Oka, M., Krucker, S., Hudson, H. S., & Saint-Hilaire, P. 2015, ApJ, 799, 129, doi: 10.1088/0004-637X/799/2/129

Patsourakos, S., Vourlidas, A., & Stenborg, G. 2013, ApJ, 764, 125, doi: 10.1088/0004-637X/764/2/125

Priest, E., & Forbes, T. 2000, Magnetic Reconnection (Cambridge University Press, Cambridge), 612

Samtaney, R., Loureiro, N. F., Uzdensky, D. A., Schekochihin, A. A., & Cowley, S. C. 2009, PhRvL, 103, 105004, doi: 10.1103/PhysRevLett.103.105004

Shen, C., Lin, J., & Murphy, N. A. 2011, ApJ, 737, 14, doi: 10.1088/0004-637X/737/1/14

Shibata, K., & Magara, T. 2011, Living Reviews in Solar Physics, 8, 6, doi: 10.12942/lrsp-2011-6

Shibata, K., Masuda, S., Shimojo, M., et al. 1995, ApJL, 451, L83, doi: 10.1086/309688

Shibata, K., & Tanuma, S. 2001, Earth, Planets, and Space, 53, 473, doi: 10.1186/BF03353258

Shimojo, M., Hudson, H. S., White, S. M., Bastian, T. S., & Iwai, K. 2017, ApJ, 841, L5, doi: 10.3847/2041-8213/aa70e3

Sturrock, P. A. 1966, Nature, 211, 695, doi: 10.1038/211695a0

Su, Y., Veronig, A. M., Holman, G. D., et al. 2013, Nature Physics, 9, 489, doi: 10.1038/nphys2675

Sun, J. Q., Cheng, X., & Ding, M. D. 2014, ApJ, 786, 73, doi: 10.1088/0004-637X/786/1/73

Uzdensky, D. A., Loureiro, N. F., & Schekochihin, A. A. 2010, Physical Review Letters, 105, 235002, doi: 10.1103/PhysRevLett.105.235002

Veronig, A. M., Brown, J. C., Dennis, B. R., et al. 2005, ApJ, 621, 482, doi: 10.1086/427274

Wang, R., Lu, Q., Du, A., & Wang, S. 2010, PhRvL, 104, 175003, doi: 10.1103/PhysRevLett.104.175003

Wu, Z., Chen, Y., Huang, G., et al. 2016, ApJL, 820, L29, doi: 10.3847/2041-8205/820/2/L29

Ye, J., Shen, C., Raymond, J. C., Lin, J., & Ziegler, U. 2019, MNRAS, 482, 588, doi: 10.1093/mnras/sty2716

Zhao, T.-L., Ni, L., Lin, J., & Ziegler, U. 2018, Research in Astronomy and Astrophysics, 18, 045, doi: 10.1088/1674-4527/18/4/45

Zhao, X., Bacchini, F., & Keppens, R. 2021, Physics of Plasmas, 28, 092113, doi: 10.1063/5.0058326

Zweibel, E. G., & Yamada, M. 2009, ARA&A, 47, 291, doi: 10.1146/annurev-astro-082708-101726